Asian Journal of Chemistry; Vol. 38, No. 9 (2026), 2281-2288
ASIAN JOURNAL OF CHEMISTRY
https://doi.org/10.14233/ajchem.2026.36311

Experimental and DFT/TD-DFT Studies of $[Ru(bbp)_2]^{2+}$ Complex: FMO Analysis and Global Reactivity Descriptors

S. ARUL MARY[1,2] and SHEEBA DANIEL[1,*]

[1]Department of Chemistry, Holy Cross College (Autonomous) (Affiliated to Manonmaniam Sundaranar University, Abishekapatti), Nagercoil-629004, India
[2]Department of Basic Engineering, Government Polytechnic College, Nagercoil-629004, India

*Corresponding author: E-mail: sheebadaniel@holycrossngl.edu.in

Received: 26 April 2026 *Accepted*: 30 June 2026 *Published online*: 5 September 2026 AJC-22456

The homoleptic ruthenium(II) complex $[Ru(bbp)_2]^{2+}$ (bbp = 2,6-*bis*(benzimidazol-2-yl)pyridine) has been synthesized and characterized by elemental analysis, UV-Visible, FTIR, ^{1}H NMR, ^{13}C NMR and MALDI-TOF-MS techniques. The spectroscopic data support coordination of the tridentate bbp ligand to the ruthenium center and formation of the proposed complex. Its electronic absorption profile features a characteristic metal-to-ligand charge-transfer (MLCT) transition arising from excitation of metal-centered orbitals to ligand-centered π*-orbitals. DFT calculations at the B3LYP/LANL2DZ level were used to examine the optimized molecular structure, frontier molecular orbitals and electronic properties, while TD-DFT calculations with an acetonitrile solvation model were employed to interpret the observed absorption features. The frontier orbital distribution places the occupied states mainly on the ruthenium center and the low-lying unoccupied states on the coordinated ligands, supporting the MLCT character of the complex. Conceptual DFT descriptors provide insight into its electronic stability, charge-transfer propensity and chemical reactivity. The combined experimental and computational study establishes a coherent relationship between the molecular structure, electronic configuration and optical response of the $[Ru(bbp)_2]^{2+}$ complex.

Keywords: Ruthenium(II) complex, 2,6-*bis*(Benzimidazol-2-yl)pyridine, DFT, Frontier molecular orbital, Global reactivity descriptors.

INTRODUCTION

Transition metal complexes constitute an important class of compounds in modern inorganic chemistry, owing to their structural diversity and rich electronic properties. They are formed through coordination of transition metal ions, which possess partially filled *d*-orbitals, with organic or inorganic ligands through coordinate covalent interactions [1]. The availability of multiple oxidation states and diverse coordination geometries gives these complexes a broad range of physicochemical properties including tunable redox behaviour, magnetic characteristics and characteristic electronic absorption features [2,3]. Among the transition-metal systems investigated extensively, ruthenium, platinum, copper and iridium complexes have attracted considerable interest due to their versatile coordination chemistry and wide range of potential chemical, photophysical and therapeutic applications.

Ruthenium(II) complexes represent an important class of coordination compounds owing to their distinctive electronic structure, coordination flexibility and rich redox chemistry. The low-spin d^6 configuration of Ru(II) favours kinetically stable octahedral architectures, while modification of the ligand environment provides effective control over the structural, electronic and photophysical characteristics of the resulting complexes [4]. Polypyridyl Ru(II) complexes are particularly notable for metal-to-ligand charge-transfer (MLCT) transitions arising from interactions between metal-centered *d*-orbitals and ligand-centered π*-orbitals. These electronic features contribute to their characteristic absorption properties and make Ru(II) complexes attractive systems for studying photoinduced electron transfer and redox processes [5,6].

Among nitrogen-donor ligands, 2,6-*bis*(benzimidazol-2-yl)pyridine (bbp) provides a rigid N,N,N-tridentate coordination environment well suited to Ru(II). The ligand combines a pyridyl donor with two benzimidazole units, forming an extended π-conjugated framework and a stable chelating environment around the metal center [7]. Coordination of ligand bbp to Ru(II) can modify the distribution of metal- and ligand-

centered electronic states, making the resulting complexes suitable for investigating the structure–property relationships through spectroscopic and computational approaches. The conjugated benzimidazole-containing framework can influence the optical and electronic response of the complex, while its multiple nitrogen donor sites support stable metal–ligand coordination [8].

The present study focuses on the synthesis and characterization of the homoleptic $[Ru(bbp)_2]^{2+}$ complex (bbp = 2,6-*bis*(benzimidazol-2-yl)pyridine), supported by a combination of spectroscopic and computational approaches. The molecular and electronic structures were investigated using density functional theory (DFT) at the B3LYP/LANL2DZ level, while time-dependent DFT (TD-DFT) calculations were employed to examine the electronic absorption characteristics and charge-transfer transitions. Frontier molecular orbital analysis was used to establish the distribution of metal- and ligand-centered electronic states and to assess the MLCT character of the complex. Conceptual DFT descriptors such as chemical potential, electronegativity, chemical hardness, softness and electrophilicity, were evaluated to gain insight into its electronic stability and reactivity. The experimental and computational findings provide insight into the structural and electronic features of $[Ru(bbp)_2]^{2+}$, linking its molecular architecture and frontier orbital distribution with its characteristic optical response.

EXPERIMENTAL

Analytical-grade solvents and chemicals (2,6-*bis*(benzimidazol-2-yl)pyridine) (bbp), $RuCl_3·3H_2O$, NH_4PF_6 and other common solvents were obtained from Sigma-Aldrich, USA.

Characterization: Elemental (CHN) analysis was carried out using a CHN elemental analyzer. The UV-Visible absorption spectral measurement was performed with a Shimadzu UV 1800 spectrometer. The FTIR spectral analysis was performed using Shimadzu FTIR double beam spectrophotometer. ^1H and ^{13}C NMR spectra were obtained from Bruker Advance III spectrometer (400 MHz) using DMSO-d_6 as the solvent at room temperature. The MALDI-TOF MS analysis was carried out to determine the *m/z* peak using Bruker Autoflex max LRF mass spectrometer instrument.

Synthesis of $[Ru(bbp)_2]^{2+}$ complex: In a round bottom flask, $RuCl_3·3H_2O$ (0.5 mmol) and lignad bbp (1 mmol) were suspended in 30 mL ethylene glycol and refluxed for 24 h under nitrogen atmosphere. After cooling, the solution was poured into aqueous NH_4PF_6 to precipitate the complex. The crude product was filtered, washed with double distilled water and diethyl ether and dried under vacuum (**Scheme-I**). Recrystallization from CH_3CN/MeOH (1:1) with 10^{-4} M aq. HPF_6 gave pure $[Ru(bbp)_2]^{2+}$ complex. Elemental analysis of $C_{38}H_{26}N_{10}Ru·2PF_6$: calcd. (found) %: C, 45.03 (45.13); H, 2.59 (2.58); N, 13.82 (13.80). The absorption maximum (λ_{max}) of $[Ru(bbp)_2]^{2+}$ complex in acetonitrile was 481 nm. FTIR (KBr pellet, cm^{-1}): 3458, 2928, 1637, 1477, 1417, 1026, 839, 573; ^1H NMR (DMSO-d_6, δ ppm): 13.77 (s, 4H, NH (imidazole)), 6.03 (d, 4H) H^9, 7.01 (t, 4H) H^8, 7.24 (t, 4H) H^7, 7.57 (d, 4H) H^6, 8.78 (t, 2H) H^1, 8.94 (d, 4H) H^2; ^{13}C NMR (DMSO-d_6, δ ppm): 119.88-157.16; MALDI-TOF-MS (*m/z*): The *m/z* values found to be at 1013.48 (M^+), 868.68 (M^+- PF_6^-) and 723.42 (M^+- $2PF_6^-$).

Computational methods: The structure of $[Ru(bbp)_2]^{2+}$ complex was initially pre-optimized using the semi-empirical MOPAC method. Subsequently, DFT and TD-DFT calculations were performed with Gaussian 09. Geometry optimization and HOMO-LUMO energy analyses were carried out employing the B3LYP functional with the LANL2DZ basis set. The optimized structure was validated through natural bond orbital (NBO) analysis and visualized using GaussView 6.0.16. Conceptual density functional theory (CDFT), grounded in the Hohenberg–Kohn theorems, was employed to derive key quantum descriptors. Chemical potential (μ), electronegativity (χ) and chemical hardness (η) were determined from energy derivatives with respect to the number of electrons. The electrophilicity index was calculated to assess the electron accepting character of the complex. Singlet excitation energies were obtained using the CPCM solvation model with acetonitrile as the solvent to examine its excited-state electronic properties.

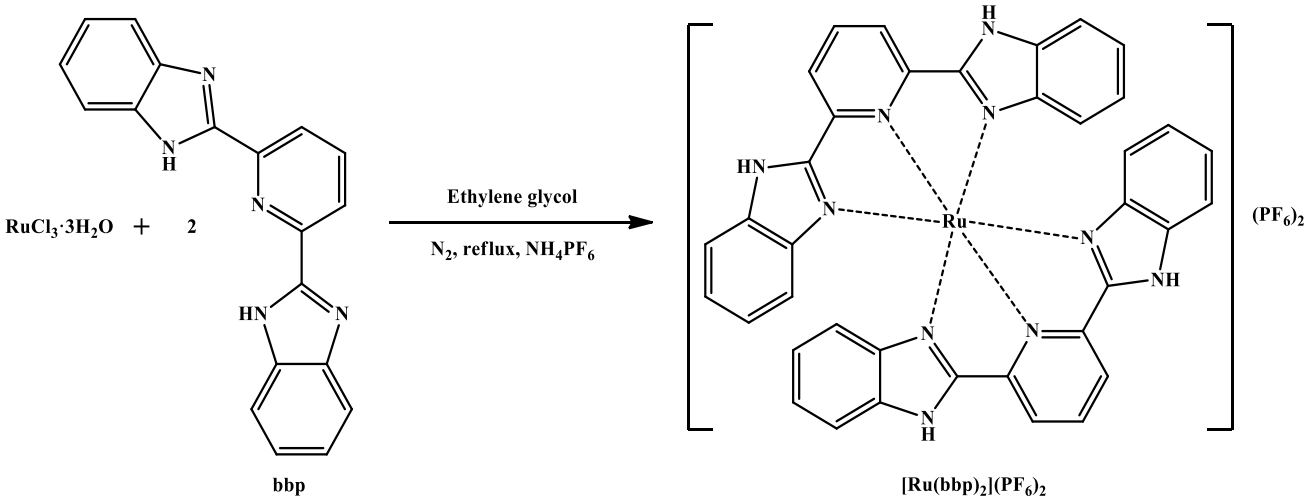

Scheme-I: Synthesis of $[Ru(bbp)_2]^{2+}$ complex

RESULTS AND DISCUSSION

The $[Ru(bbp)_2]^{2+}$ complex was synthesized by refluxing $RuCl_3 \cdot 3H_2O$ with two equivalents of 2,6-*bis*(benzimidazol-2-yl)pyridine (bbp) ligand in ethylene glycol under a nitrogen atmosphere, followed by precipitation with NH_4PF_6, as outlined in **Scheme-I**. The isolated complex is readily soluble in acetonitrile, DMF and DMSO and exhibited an intense colouration. Elemental analysis showed close agreement between the experimental and calculated C, H and N values for $C_{38}H_{26}N_{10}Ru \cdot 2PF_6$ [9].

Absorption spectral analysis: The UV-Visible spectrum of $[Ru(bbp)_2]^{2+}$ recorded in acetonitrile exhibits absorption bands at 258, 312, 330, 350 and 481 nm (Fig. 1). The low-energy band at 481 nm is assigned to a metal-to-ligand charge transfer (MLCT) transition involving promotion of electron density from Ru(dπ) orbitals to the ligand-centered π∗ orbitals [10]. The higher-energy bands at 258 and 312 nm are attributed to ligand-centered π→π* transitions, while the bands in the 330-350 nm region are assigned to intraligand charge-transfer (ILCT) transitions within the coordinated bbp ligand [11].

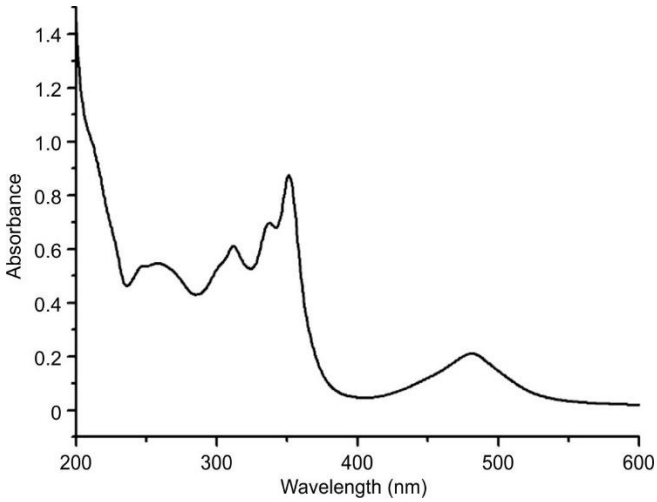

Fig. 1. UV-Visible spectrum of $[Ru(bbp)_2]^{2+}$ complex

FTIR spectral analysis: The FTIR spectrum of $[Ru(bbp)_2]^{2+}$ (Fig. 2) exhibits characteristic vibrational bands associated with the coordinated bbp ligand and PF_6^- counterions. The broad band at 3458 cm^{-1} is assigned to N–H stretching, while the band at 2928 cm^{-1} corresponds to C–H stretching vibrations of the aromatic rings [12]. The band at 1637 cm^{-1} is attributed to the C=N stretching vibration of the benzimidazole units. Bands at 1477 and 1417 cm^{-1} arise mainly from the aromatic ring vibrations [13]. The band at 1026 cm^{-1} can be assigned to a pyridine ring-breathing vibration, while the weak band at 573 cm^{-1} is associated with Ru–N stretching. The strong band at 839 cm^{-1} is characteristic of the PF_6^- anion [14]. These vibrational features are consistent with coordination of bbp to Ru(II) and the presence of PF_6^- counterions.

^{1}H NMR spectral analysis: The ^{1}H NMR spectrum of $[Ru(bbp)_2]^{2+}$ recorded in DMSO-d_6 is shown in Fig. 3a. The spectrum exhibits well-resolved resonances corresponding to the aromatic protons of the coordinated bbp ligands. The signal

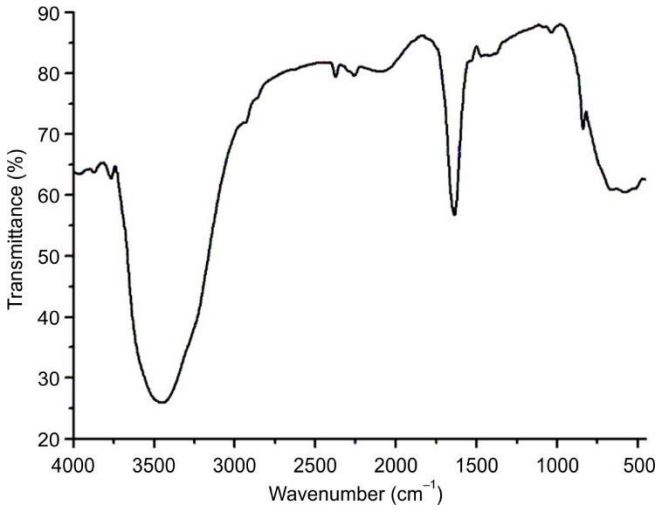

Fig. 2. FTIR spectrum of $[Ru(bbp)_2]^{2+}$ complex

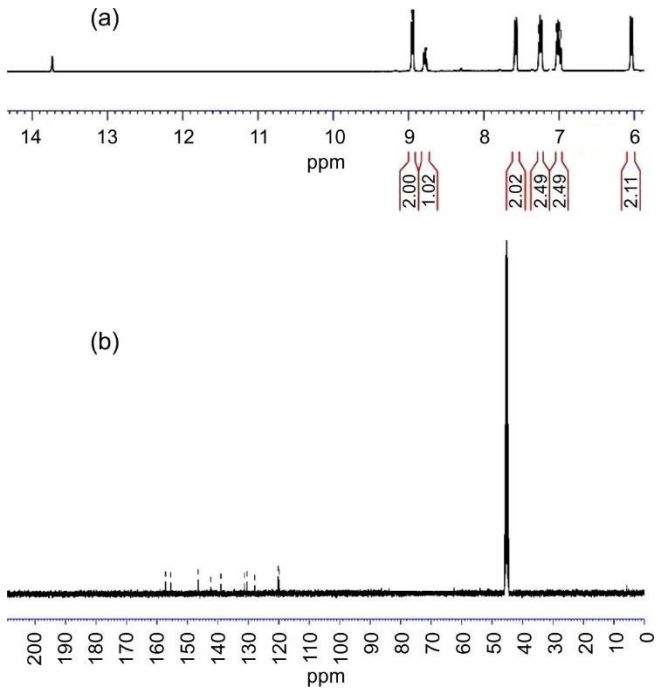

Fig. 3. (a) ^{1}H NMR and (b) ^{13}C NMR spectra of $[Ru(bbp)_2]^{2+}$ complex

at δ 13.77 ppm is assigned to the imidazole N–H protons. Its pronounced downfield position can be associated with hydrogen bonding involving the N–H groups and the DMSO solvent [15]. The aromatic proton resonances occur in the δ 6.03-8.94 ppm region. The H^1 resonance appears at δ 8.78 ppm, while H^2 gives a doublet at δ 8.94 ppm. Signals assigned to H^6 and H^7 occur at δ 7.57 and 7.24 ppm, respectively. The resonances of H^8 and H^9 appear at δ 7.01 and 6.03 ppm. The chemical shift changes observed for the pyridine and benzimidazole protons are consistent with coordination-induced changes in the electronic environment of the ligand [16,17]. In particular, the altered resonance positions of the protons adjacent to the coordinating nitrogen atoms reflect the effect of Ru(II) coordination on the ligand π-system. The observed proton resonances are consistent with the proposed coordination environment of the $[Ru(bbp)_2]^{2+}$ complex.

^{13}C spectral analysis: The ^{13}C NMR spectrum of Ru complex recorded in DMSO-d_6 is shown in Fig. 3b. The resonances extend from δ 119.88 to 157.16 ppm, consistent with the aromatic carbon framework of the coordinated bbp ligands. The downfield signals at δ 157.16 and 155.49 ppm are assigned to C4 and C3, respectively, which are positioned adjacent to the coordinating nitrogen atoms. Their deshielding can be associated with Ru–N coordination and the accompanying redistribution of electron density arising from Ru←N σ-donation [16]. The signals at δ 146.50 and 142.36 ppm are attributed to the benzimidazole quaternary carbons C5 and C10, influenced by the adjacent nitrogen atoms and extended π-conjugation [18]. The pyridine C1 carbon appears at δ 139.02 ppm, while C2 and the benzimidazole aromatic carbons C6–C9 resonate between δ 119.88 and 131.26 ppm. The observed chemical shift pattern reflects the electronic influence of Ru(II) coordination on the bbp framework and supports the proposed structure of $[Ru(bbp)_2]^{2+}$ [19].

Mass spectral analysis: The MALDI-TOF mass spectrum of $[Ru(bbp)_2]^{2+}$ (Fig. 4) displays a molecular ion peak at *m/z* 1013.48, consistent with the proposed molecular composition containing two PF_6^- counterions. Fragment peaks at *m/z* 868.68 and 723.42 are attributed to the successive loss of one and two PF_6^- ions, respectively. Such fragmentation is consistent with PF_6^- containing Ru(II) coordination complexes [14]. The experimentally observed molecular mass shows close agreement with the calculated mass of the proposed complex.

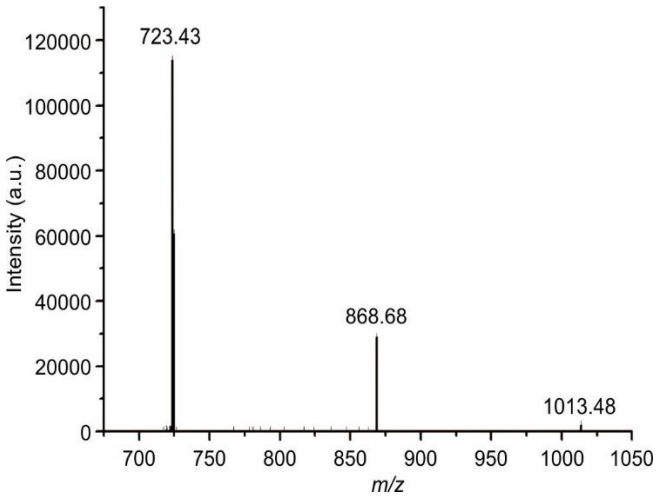

Fig. 4. MALDI-TOF mass spectrum of $[Ru(bbp)_2]^{2+}$ complex

DFT ground-state geometry: Density functional theory (DFT) was employed to optimize the ground-state geometry and determine the structural parameters of the complex, providing insight into its bonding characteristics and frontier molecular orbitals.

Ground-state structural properties: The ground-state geometry of $[Ru(bbp)_2]^{2+}$ was optimized in the gas phase using Gaussian 09W and the optimized structure is shown in Fig. 5. The calculated bond lengths and bond angles are listed in Tables 1 and 2, respectively. Bond length represents the average distance between the nuclei of two bonded atoms in a molecule [20].

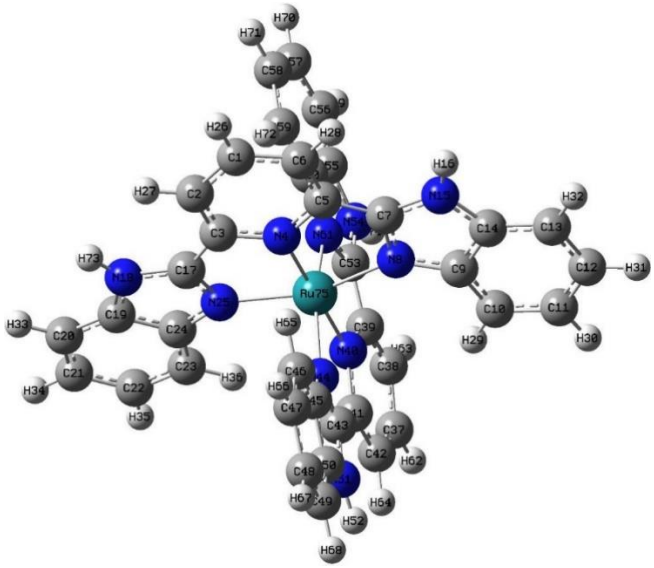

Fig. 5. Optimized geometry of $[Ru(bbp)_2]^{2+}$ complex obtained at B3LYP/LANL2DZ

In $[Ru(bbp)_2]^{2+}$ complex, C=C bond lengths range from 1.4017 Å to 1.4187 Å (Table-1). However, bonds like C_3–C_{17}, C_5–C_7, C_9–C_{14}, C_{19}–C_{24}, C_{39}–C_{53}, C_{41}–C_{43}, C_{45}–C_{50} and C_{55}–C_{60} exhibit slightly longer (~1.43 Å) due to adjacent electronegative nitrogen atoms. Ru–N bond lengths fall between 2.02 Å and 2.1016 Å, aligning closely with values from previously reported complexes [21]. Table-2 presents the bond angles for $[Ru(bbp)_2]^{2+}$ complex. The divalent metal center coordinates with a tridentate ligand, resulting in a distorted octahedral geometry. The chelate bite angles range from 77.87º to 77.94º. Although, the inter-ligand trans angle N4–Ru–N40 is 179.95º, corresponding to an almost linear arrangement, whereas the intra-ligand N8–Ru–N25 and N44–Ru–N61 angles are 157.82º, reflecting the geometric constraints of the tridentate ligand framework. The calculated bond angles are comparable to those reported for related Ru(II) complexes [22].

Frontier molecular orbital (FMO) analysis using DFT: Molecular orbital composition analysis shows that the occupied orbitals from HOMO–4 to HOMO are predominantly metal centered, with Ru(d) contributions of approximately 57-68% [23]. The HOMO contains about 62% Ru(d) character with a partial ligand contribution. In contrast, the unoccupied orbitals from LUMO to LUMO+4 are mainly ligand-centered, with the LUMO containing approximately 92% ligand π* character [24]. The FMOs of $[Ru(bbp)_2]^{2+}$ are shown in Fig. 6. The separation of metal-centered occupied orbitals and ligand-centered unoccupied orbitals supports a metal-to-ligand charge transfer (MLCT) process involving excitation from Ru(d) orbitals to ligand π*-orbitals. This orbital distribution provides insight into the electronic structure, charge-transfer characteristics and reactivity of the complex.

TD-DFT studies: In the present study, TD-DFT calculations were performed for $[Ru(bbp)_2]^{2+}$ complex at B3LYP/LANL2DZ level using the CPCM solvation model in acetonitrile to explore the electronic absorption behaviour of the complex. The experimental and TD-DFT calculated absorption data are listed in Table-3. TD-DFT calculations reveal several singlet excited states that contribute to the electronic

TABLE-1
BOND LENGTH OF $[Ru(bbp)_2]^{2+}$ COMPLEX BY B3LYP/LANL2DZ DFT CALCULATIONS

Atoms	Bond length (Å)	Atoms	Bond length (Å)	Atoms	Bond length (Å)	Atoms	Bond length (Å)
C_1-C_2	1.4175	C_{12}-C_{13}	1.4098	C_{37}-C_{38}	1.4175	C_{48}-C_{49}	1.4098
C_1-C_6	1.4187	C_{12}-H_{31}	1.0874	C_{37}-C_{42}	1.4187	C_{48}-H_{67}	1.0874
C_1-H_{26}	1.0858	C_{13}-C_{14}	1.4027	C_{37}-H_{62}	1.0858	C_{49}-C_{50}	1.4027
C_2-C_3	1.4024	C_{13}-H_{32}	1.0869	C_{38}-C_{39}	1.4024	C_{49}-H_{68}	1.0869
C_2-H_{27}	1.0878	C_{14}-N_{15}	1.4014	C_{38}-H_{63}	1.0878	C_{50}-N_{51}	1.4014
C_3-N_4	1.3999	N_{15}-H_{16}	1.0089	C_{39}-N_{40}	1.3999	N_{51}-H_{52}	1.0089
C_3-C_{17}	1.4344	C_{17}-N_{18}	1.3977	C_{39}-C_{53}	1.4344	C_{53}-N_{54}	1.3977
N_4-C_5	1.398	C_{17}-N_{25}	1.3742	N_{40}-C_{41}	1.3980	C_{53}-N_{61}	1.3742
N_4-Ru_{75}	2.0200	N_{18}-C_{19}	1.4015	N_{40}-Ru_{75}	2.0200	N_{54}-C_{55}	1.4015
C_5-C_6	1.4017	N_{18}-H_{73}	1.0089	C_{41}-C_{42}	1.4017	N_{54}-H_{74}	1.0089
C_5-C_7	1.4359	C_{19}-C_{20}	1.4025	C_{41}-C_{43}	1.4359	C_{55}-C_{56}	1.4025
C_6-H_{28}	1.0877	C_{19}-C_{24}	1.4310	C_{42}-H_{64}	1.0877	C_{55}-C_{60}	1.4310
C_7-N_8	1.3732	C_{20}-C_{21}	1.4101	C_{43}-N_{44}	1.3731	C_{56}-C_{57}	1.4101
C_7-N_{15}	1.3971	C_{20}-H_{33}	1.0870	C_{43}-N_{51}	1.3971	C_{56}-H_{69}	1.0870
N_8-C_9	1.399	C_{21}-C_{22}	1.4179	N_{44}-C_{45}	1.3990	C_{57}-C_{58}	1.4179
N_8-Ru_{75}	2.1015	C_{21}-H_{34}	1.0874	N_{44}-Ru_{75}	2.1016	C_{57}-H_{70}	1.0874
C_9-C_{10}	1.407	C_{22}-C_{23}	1.4063	C_{45}-C_{46}	1.4070	C_{58}-C_{59}	1.4063
C_9-C_{14}	1.4309	C_{22}-H_{35}	1.0873	C_{45}-C_{50}	1.4308	C_{58}-H_{71}	1.0873
C_{10}-C_{11}	1.4060	C_{23}-C_{24}	1.4071	C_{46}-C_{47}	1.4060	C_{59}-C_{60}	1.4071
C_{10}-H_{29}	1.0851	C_{23}-H_{36}	1.0851	C_{46}-H_{65}	1.0851	C_{59}-H_{72}	1.0851
C_{11}-C_{12}	1.4181	C_{24}-N_{25}	1.3986	C_{47}-C_{48}	1.4181	C_{60}-N_{61}	1.3986
C_{11}-H_{30}	1.0873	N_{25}-Ru_{75}	2.1003	C_{47}-H_{66}	1.0873	N_{61}-Ru_{75}	2.1002

TABLE-2
BOND ANGLE OF $[Ru(bbp)_2]^{2+}$ COMPLEX BY B3LYP/LANL2DZ DFT CALCULATIONS

Atoms	Bond angle (°)	Atoms	Bond angle (°)	Atoms	Bond angle (°)	Atoms	Bond angle (°)
A(2,1,6)	120.2421	A(9,14,15)	105.8884	A(40,39,53)	110.2941	A(53,54,55)	108.2044
A(2,1,26)	119.8821	A(13,14,15)	132.1248	A(39,40,41)	120.9723	A(53,54,74)	125.5321
A(6,1,26)	119.8758	A(7,15,14)	108.1893	A(39,40,75)	119.4526	A(55,54,74)	126.2366
A(1,2,3)	119.4248	A(7,15,16)	125.5306	A(41,40,75)	119.575	A(54,55,56)	132.1189
A(1,2,27)	119.8444	A(14,15,16)	126.2592	A(40,41,42)	120.0829	A(54,55,60)	105.8981
A(3,2,27)	120.7279	A(3,17,18)	130.8268	A(40,41,43)	110.2543	A(56,55,60)	121.9829
A(2,3,4)	119.9401	A(3,17,25)	119.1632	A(42,41,43)	129.5049	A(55,56,57)	117.0843
A(2,3,17)	129.6114	A(18,17,25)	109.8457	A(37,42,41)	119.3335	A(55,56,69)	121.8928
A(4,3,17)	110.2934	A(17,18,19)	108.2041	A(37,42,64)	119.8811	A(57,56,69)	121.0222
A(3,4,5)	120.9723	A(17,18,73)	125.532	A(41,42,64)	120.7822	A(56,57,58)	121.3303
A(3,4,75)	119.4551	A(19,18,73)	126.2369	A(41,43,44)	119.1514	A(56,57,70)	119.2905
A(5,4,75)	119.5726	A(18,19,20)	132.1193	A(41,43,51)	130.7816	A(58,57,70)	119.3787
A(4,5,6)	120.0804	A(18,19,24)	105.8978	A(44,43,51)	109.9105	A(57,58,59)	121.4437
A(4,5,7)	110.255	A(20,19,24)	121.9829	A(43,44,45)	107.0848	A(57,58,71)	119.1773
A(6,5,7)	129.5067	A(19,20,21)	117.084	A(43,44,75)	112.8729	A(59,58,71)	119.3784
A(1,6,5)	119.3352	A(19,20,33)	121.893	A(45,44,75)	139.9826	A(58,59,60)	117.8215
A(1,6,28)	119.8804	A(21,20,33)	121.0223	A(44,45,46)	130.7475	A(58,59,72)	121.7872
A(5,6,28)	120.7812	A(20,21,22)	121.3307	A(44,45,50)	108.9078	A(60,59,72)	120.3914
A(5,7,8)	119.1517	A(20,21,34)	119.2904	A(46,45,50)	120.343	A(55,60,59)	120.3356
A(5,7,15)	130.7821	A(22,21,34)	119.3784	A(45,46,47)	117.8163	A(55,60,61)	108.9132
A(8,7,15)	109.9096	A(21,22,23)	121.4436	A(45,46,65)	120.3972	A(59,60,61)	130.7492
A(7,8,9)	107.085	A(21,22,35)	119.1773	A(47,46,65)	121.7864	A(53,61,60)	107.117
A(7,8,75)	112.8725	A(23,22,35)	119.3786	A(46,47,48)	121.4417	A(53,61,75)	112.8615
A(9,8,75)	139.9827	A(22,23,24)	117.8212	A(46,47,66)	119.3836	A(60,61,75)	139.9518
A(8,9,10)	130.7478	A(22,23,36)	121.7876	A(48,47,66)	119.1742	A(4,75,8)	77.8806
A(8,9,14)	108.908	A(24,23,36)	120.3912	A(47,48,49)	121.3399	A(4,75,25)	77.9397
A(10,9,14)	120.3425	A(19,24,23)	120.3361	A(47,48,67)	119.3687	A(4,75,44)	102.0747
A(9,10,11)	117.8166	A(19,24,25)	108.9131	A(49,48,67)	119.2909	A(4,75,61)	102.1051
A(9,10,29)	120.3974	A(23,24,25)	130.7489	A(48,49,50)	117.071	A(8,75,25)	155.82
A(11,10,29)	121.786	A(17,25,24)	107.1167	A(48,49,68)	121.0301	A(8,75,40)	102.072
A(10,11,12)	121.4417	A(17,25,75)	112.862	A(50,49,68)	121.8983	A(8,75,44)	93.2573
A(10,11,30)	119.3835	A(24,25,75)	139.9517	A(45,50,49)	121.9867	A(8,75,61)	91.8767

A(12,11,30)	119.1743	A(38,37,42)	120.2421	A(45,50,51)	105.8881	A(25,75,40)	102.1078
A(11,12,13)	121.3396	A(38,37,62)	119.8822	A(49,50,51)	132.1252	A(25,75,44)	91.8752
A(11,12,31)	119.369	A(42,37,62)	119.8757	A(43,51,50)	108.189	A(25,75,61)	93.0482
A(13,12,31)	119.291	A(37,38,39)	119.4264	A(43,51,52)	125.5306	A(40,75,44)	77.8793
A(12,13,14)	117.0713	A(37,38,63)	119.8437	A(50,51,52)	126.2595	A(40,75,61)	77.941
A(12,13,32)	121.03	A(39,38,63)	120.727	A(39,53,54)	130.8272	A(44,75,61)	155.82
A(14,13,32)	121.898	A(38,39,40)	119.9377	A(39,53,61)	119.1635	A(4,75,40)	179.95
A(9,14,13)	121.9868	A(38,39,53)	129.6132	A(54,53,61)	109.8448		

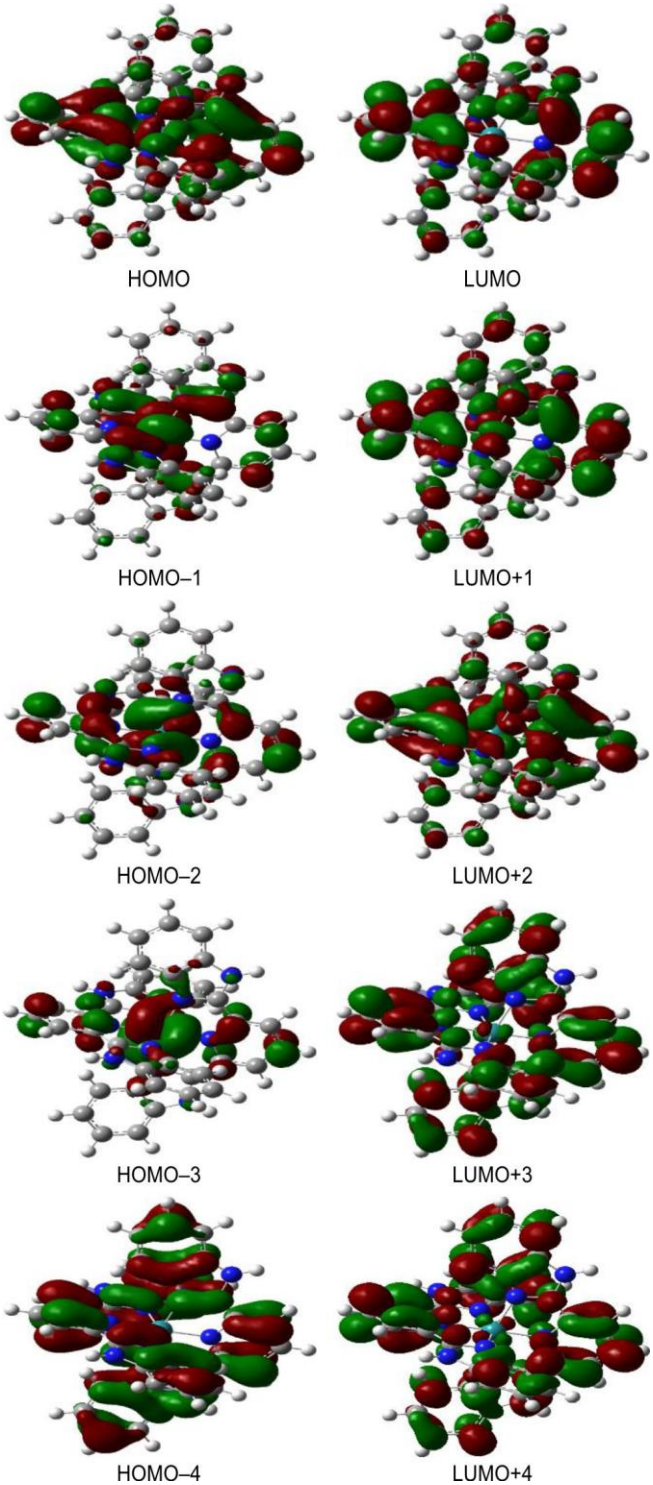

Fig. 6. DFT-B3LYP/LANL2DZ calculated frontier molecular orbitals (FMO) of the $[Ru(bbp)_2]^{2+}$ complex

absorption spectrum of the Ru(II) complex. The absorption band at 450.46 nm (2.7524 eV) originates from mixed electronic transitions, primarily HOMO-2→LUMO+1 (22.17%) and HOMO-1→LUMO (22.14%), with a minor contribution from HOMO→LUMO+2 (4.35%). This band corresponds to the experimentally observed metal-to-ligand charge transfer (MLCT), confirming its charge-transfer character. A prominent excited state at 354 nm (3.50 eV) is mainly associated with the HOMO-3→LUMO+1 transition, which contributes 47.85% of the excitation. Similarly, the absorption band at 340.96 nm (3.6363 eV) is predominantly governed by the HOMO-4→LUMO transition (47.89%) with a minor contribution from HOMO-3→LUMO+1 (1.10%). The higher-energy transition at 312.81 nm (3.9636 eV) exhibits a mixed electronic nature, involving mainly HOMO-6→LUMO+2 (24.52%) and HOMO-5→LUMO+3 (15.72%) excitations [25]. Other electronic configurations contribute less than 3% to the corresponding excitation weights. The calculated absorption maxima differ from the experimental bands by approximately 10-31 nm, with reasonable agreement between the theoretical and experimental spectra (Fig. 7). The calculated transitions reproduce the principal features of the experimental absorption profile and support the assignment of the electronic transitions in the Ru(II) complex.

FMO analysis shows that the highest occupied molecular orbital (HOMO) is primarily localized on the ruthenium center with dominant Ru(d) character, whereas the lowest unoccupied molecular orbitals (LUMO and LUMO+1) are mainly distributed over the π*-orbitals of the coordinated ligands. This spatial separation of electron density supports the MLCT character of the low-energy transitions, with excitation from metal centered *d*-orbitals to ligand-centered π*-orbitals [26].

Global reactivity descriptors: The HOMO and LUMO energies of $[Ru(bbp)_2]^{2+}$ were calculated as -10.3093 and -7.4053 eV, respectively, giving a HOMO–LUMO gap of 2.904 eV (Fig. 8). The occupied orbitals possess predominantly Ru(d) character, whereas the unoccupied orbitals are mainly ligand-centered π*-states, consistent with the MLCT transitions obtained from the TD-DFT analysis [27].

The calculated global reactivity descriptors are presented in Table-4. Based on Koopmans' theorem, the ionization potential and electron affinity were estimated as 10.3093 and 7.4053 eV, respectively. The electronegativity and chemical potential were calculated as 8.8573 and -8.8573 eV. The chemical hardness and softness were calculated as 1.452 eV and 0.3443 eV^{-1}, respectively, providing insight into the electronic response of the complex to changes in electron density [28]. The electrophilicity index of 27.0150 eV reflects a pronounced electron-accepting character. These parameters describe the electronic stability and reactivity of $[Ru(bbp)_2]^{2+}$ complex.

TABLE-3
EXPERIMENTAL AND THEORETICAL UV-VISIBLE ABSORPTION DATA OF THE $[Ru(bbp)_2]^{2+}$ COMPLEX

Wavelength (nm)		Oscillator strength (f)	Major transitions	
Experimental	Theoretical		Excited sates	HOMO→LUMO
312	312.81	0.162	37	HOMO-6→LUMO+2 (24.52%) HOMO-5→LUMO+3 (15.72%)
330	340.96	0.186	16	HOMO-4→LUMO (47.89%) HOMO-3→LUMO+1 (1.10%)
350	354.00	0.2273	15	HOMO-3→LUMO+1 (47.85%)
481	450.46	0.1682	7	HOMO-2→LUMO+1 (22.17%) HOMO-1→LUMO (22.14%) HOMO→LUMO+2 (4.35%)

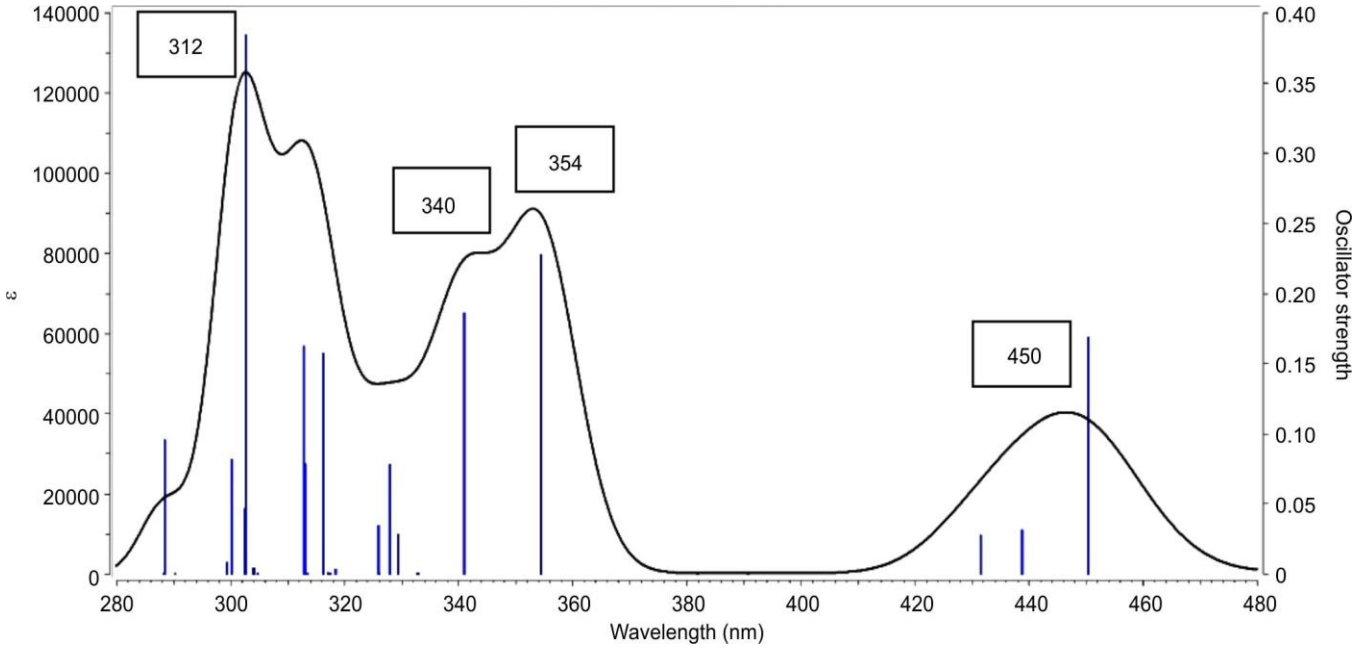

Fig. 7. Computed absorption spectra, vertical excitation energies and oscillator strengths of the $[Ru(bbp)_2]^{2+}$ complex

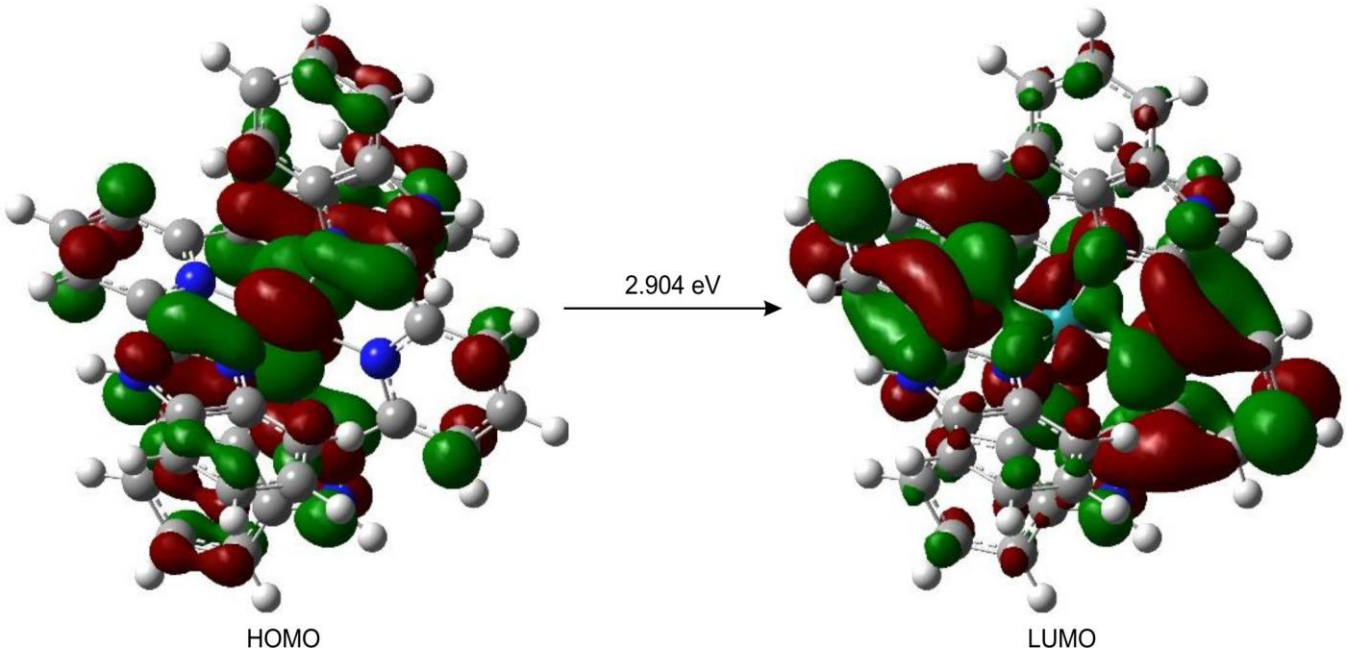

Fig. 8. Energy level diagram for $[Ru(bbp)_2]^{2+}$ complex

TABLE-4
GLOBAL REACTIVITY DESCRIPTORS
OF $[Ru(bbp)_2]^{2+}$ COMPLEX

Parameters	Theoretical values (eV)
E_{HOMO}	-10.3093
E_{LUMO}	-7.4053
Energy gap (ΔE)	2.904
Ionization potential (I)	10.3093
Electron affinity (A)	7.4053
Electronegativity (χ)	8.8573
Chemical potential (μ)	-8.8573
Hardness (η)	1.452
Softness (σ)	0.3443
Electrophilicity index (ω)	27.01507

Conclusion

The homoleptic $[Ru(bbp)_2]^{2+}$ complex was synthesized and characterized by elemental analysis, UV-Visible spectroscopy, FTIR, ^1H NMR, ^{13}C NMR and MALDI-TOF mass spectrometry, with the combined data supporting the proposed molecular structure. Theoretical investigations using DFT and TD-DFT provide valuable insights into the electronic structure, frontier molecular orbitals and excited-state transitions. Electronic absorption spectroscopy reveals a prominent metal-to-ligand charge transfer (MLCT) band at 481 nm, which is excellently rationalized by TD-DFT calculations. The simulated spectrum successfully assigns this intense transition at 450.46 nm (2.7524 eV) showing it originates from mixed electronic transitions, primarily HOMO-2→LUMO+1 (22.17%) and HOMO-1→LUMO (22.14%), with a minor contribution from HOMO→LUMO+2 (4.35%). The calculated HOMO-LUMO energy gap of 2.904 eV indicates favourable electronic stability and efficient charge-transfer behaviour. The global reactivity descriptors reveal the chemical stability, reactivity trends and potential charge-transfer capabilities of the complex. The combined experimental and computational findings link the molecular structure and frontier orbital distribution of $[Ru(bbp)_2]^{2+}$ with its optical response, providing a basis for further photophysical and electronic studies.

CONFLICT OF INTEREST

The authors declare that there is no conflict of interests regarding the publication of this article.

DECLARATION OF AI-ASSISTED TECHNOLOGIES

During the preparation of this manuscript, the authors used an AI-assisted tool(s) to improve the language and no data, results or scientific conclusions were generated by AI. All analyses, interpretations and conclusions are the authors' own. The authors reviewed and edited the content and take full responsibility for the published work.

REFERENCES

1. J.W. Toney, R.G. St. Michel, A.G. Garrison, I. Kevlishvili and H.J. Kulik, *Proc. Natl. Acad. Sci. USA*, **122**, 1 (2025); https://doi.org/10.1073/pnas.2415658122
2. A. Markovic, L. Gerhards, P. Sander, C. Dosche, T. Klüner, R. Beckhaus and G. Wittstock, *Chemphyschem*, **21**, 2506 (2020); https://doi.org/10.1002/cphc.202000547
3. C.M. Dickie, A.L. Laughlin, J.D. Wofford, N.S. Bhuvanesh and M. Nippe, *Chem. Sci.*, **8**, 8039 (2017); https://doi.org/10.1039/C7SC03380J
4. Y. Yang, G. Liao and C. Fu, *Polymers*, **10**, 650 (2018); https://doi.org/10.3390/polym10060650
5. G. Lemercier, A. Bonne, M. Four and L.M. Lawson-Daku, *C.R. Chim.*, **11**, 709 (2008); https://doi.org/10.1016/j.crci.2007.11.012
6. I. Kacsir, A. Sipos, A. Bényei, E. Janka, P. Buglyó, L. Somsák, P. Bai and É. Bokor, *Int. J. Mol. Sci.*, **23**, 813 (2022); https://doi.org/10.3390/ijms23020813
7. Z. Šindelar and P. Kopel, *Inorganics*, **11**, 113 (2023); https://doi.org/10.3390/inorganics11030113
8. J. Wang, L. Shuai, X. Xiao, Y. Zeng, Z. Li and T. Matsumura-Inoue, *J. Inorg. Biochem.*, **99**, 883 (2005); https://doi.org/10.1016/j.jinorgbio.2004.12.018
9. M. Fuster, I. Moulefera, M.G. Montalbán, J. Pérez, G. Víllora and G. García, *Molecules*, **27**, 7264 (2022); https://doi.org/10.3390/molecules27217264
10. S.J. Steinke, S. Gupta, E.J. Piechota, C.E. Moore, J.J. Kodanko and C. Turro, *Chem. Sci.*, **13**, 1933 (2022); https://doi.org/10.1039/D1SC05647F
11. M. Shiotsuka, Y. Tsuji, K. Keyaki and K. Nozaki, *Inorg. Chem.*, **49**, 4186 (2010); https://doi.org/10.1021/ic902417m
12. S.Y. Wei, J.L. Wang, C.S. Zhang, X.T. Xu, X.X. Zhang, J.X. Wang and Y.H. Xing, *ChemPlusChem*, **80**, 549 (2015); https://doi.org/10.1002/cplu.201402255
13. G.S. Fasiuddin, A.A. Basha, A. Kubaib, S. Khasim, G. Bouzid, A. Almasoudi and M.R. Ajmal, *Sci. Rep.*, **15**, 44010 (2025); https://doi.org/10.1038/s41598-025-27674-7
14. T. Ezhilarasu and S. Balasubramanian, *ChemistrySelect*, **3**, 12039 (2018); https://doi.org/10.1002/slct.201801624
15. S.H. Jawad and K.J. Al-adilee, *Results Chem.*, **4**, 100573 (2022); https://doi.org/10.1016/j.rechem.2022.100573
16. A.E. Ceniceros-Gómez, A. Ramos-Organillo, J. Hernández-Díaz, J. Nieto-Martínez, R. Contreras and S.E. Castillo-Blum, *Heteroatom Chem.*, **11**, 392 (2000); https://doi.org/10.1002/1098-1071(2000)11:6<392::AID-HC6>3.0.CO;2-G
17. D. Maity, C. Bhaumik, D. Mondal and S. Baitalik, *Inorg. Chem.*, **52**, 13941 (2013); https://doi.org/10.1021/ic401582m
18. V. Antoci, D. Cucu, G. Zbancioc, C. Moldoveanu, V. Mangalagiu, D. Amariucai-Mantu, A. Aricu and I.I. Mangalagiu, *Future Med. Chem.*, **12**, 207 (2020); https://doi.org/10.4155/fmc-2019-0063
19. X. Xiaoming, M. Haga, T. Matsumura-Inoue, Y. Ru, A.W. Addison and K. Kano, *J. Chem. Soc., Dalton Trans.*, **3**, 2477 (1993); https://doi.org/10.1039/dt9930002477
20. J. Brindha, S.M. Rani, V.S. Chithra and T.F.A.F. Reji, *Indian J. Chem.*, **58B**, 1063 (2019).
21. S. David, R.S. Perkins, F.R. Fronczek, S. Kasiri, S.S. Mandal and R.S. Srivastava, *J. Inorg. Biochem.*, **111**, 33 (2012); https://doi.org/10.1016/j.jinorgbio.2012.02.022
22. C. Bhaumik, D. Saha, S. Das and S. Baitalik, *Inorg. Chem.*, **50**, 12586 (2011); https://doi.org/10.1021/ic201610w
23. D. Saha, S. Das, S. Karmakar, S. Dutta and S. Baitalik, *RSC Adv.*, **3**, 17314 (2013); https://doi.org/10.1039/c3ra41114a
24. E.C. Constable, M. Devereux, E.L. Dunphy, C.E. Housecroft, J.A. Rudd and J.A. Zampese, *Dalton Trans.*, **40**, 5505 (2011); https://doi.org/10.1039/c0dt01714k
25. B.B. Cui, J.Y. Shao and Y.W. Zhong, *Organometallics*, **33**, 4220 (2014); https://doi.org/10.1021/om500486v
26. D. Mondal, P. Pal and S. Baitalik, *Sens. Actuators B Chem.*, **242**, 746 (2017); https://doi.org/10.1016/j.snb.2016.11.058
27. A.O. Zacharias, A. Varghese, K.B. Akshaya, M.S. Savitha and L. George, *J. Mol. Struct.*, **1158**, 1 (2018); https://doi.org/10.1016/j.molstruc.2018.01.002
28. M. Muthukkumar, C. Kamal, G. Venkatesh, C. Kaya, S. Kaya, I.V.M.V. Enoch, P. Vennila and R. Rajavel, *J. Mol. Struct.*, **1147**, 502 (2017); https://doi.org/10.1016/j.molstruc.2017.06.132